SPH MODELLING OF COHERENT STRUCTURES AND INTERMITTENT EVENTS IN THE SURF ZONE OF WEAK PLUNGERS

CHRISTOS V. MAKRIS[(1)], YANNIS N. KRESTENITIS [(1)] & CONSTANTINE D. MEMOS [(2)]

[(1)]   *Dept. of Civil Engineering, Aristotle University of Thessaloniki, Thessaloniki, Greece,*
cmakris@civil.auth.gr, ynkrest@civil.auth.gr

[(2)]   *School of Civil Engineering, National Technical University of Athens,Athens, Greece,*
memos@hydro.ntua.gr

ABSTRACT

The prime goal of the present study is the detailed numerical simulation of surf zone hydrodynamics, due to weakly plunging breakers on a relatively mild impermeable slope. Smoothed Particle Hydrodynamics method is used in combination with a Smagorinsky-type model for the sub-particle scales of the flow, similarly to a Large Eddy Simulations' approach; hence the academic 'open-source' code SPHysics is implemented. We undertake thorough pre-processing analysis of experimental eddy sizes in regular wave breaking and thus choose a spatial resolution approaching the demarcation point between integral turbulence length scales and Taylor micro-scales. Moreover, a combination of heuristic techniques for the discrimination of turbulent fluctuations from the ordered wave motion is proposed as a post-processing manipulation of SPH Lagrange-type data. The model is validated against experimental data, concerning several wave features. Spectral analysis of the fluctuating components for the velocity field is used to investigate its isotropic substance. Results in the surf zone concern wave-induced mean flows, dynamic characteristics of weak plungers and consequent bores, coherent structures on vertical cross-sections, and intermittent events at fixed gauges. The recurring patterns of vorticity are studied both in Eulerian and Lagrangian perspective, and reveal plausible reproduction of classic coherent vortical structures, which define the topology and properties of the wave breaking mechanism. The latter is supported by the derivation of coherent structures of turbulent kinetic energy (TKE) and Reynolds stresses, too. Additionally, the cross-shore variation of intermittent fluctuations due to wave breaking is investigated by empirical identification of coherent and intense events. The statistics of intermittency agree with experimental data; e.g. coherent intermittent events occur only for a small portion (<20%) of the TKE time-series, but contribute significantly to its magnitude by containing a significant amount (>50%) of all motions. Correlations between shear stresses and TKE are detected, allowing us to define possible cross-shore sediment transport patterns related to them.

Keywords: Surf zone; SPH; coherent structures; intermittent events; weak plunging breakers

1.   INTRODUCTION

Near-shore wave breaking is one of the most significant processes for coastal engineers and scientists in their endeavour to determine the surf and swash zone dynamics. Nevertheless, the highly turbulent regime of the respective flows renders the underlying hydrodynamics far from completely elucidated. For example, there is still no 'clean' definition of the turbulent characteristics for breaking waves, i.e. a proper and robust discrimination of turbulent fluctuations from the ordered wave motion through a certain averaging method. There is still a lot of discussion taking place on the definition of coherent structures (based on vorticity or other turbulent features), and the description of intermittent events of turbulent nature, which primarily control sediment movements and cross-shore morphodynamic evolution. In this direction, the past research endeavours concentrated mostly on the physical and numerical modelling of instantaneous and phase- or ensemble-averaged values for various fluid properties. Such factors are the free surface elevation η, the vertically distributed and the depth-averaged velocities **u** and U, the wave-induced currents, the vorticity ω, the fluctuating components of horizontal and vertical velocities u' and w' (i.e. $u=\bar{u}+u'$, u is fluid velocity and $\bar{u}$ is averaged velocity), the turbulent kinetic energy (TKE) $k=(u'^2+w'^2)/2$, the shear and normal stresses $\tau_{ss}=-\rho u'w'$ and $\tau_{nx}=\rho u'^2$ or $\tau_{nz}=\rho w'^2$ respectively (ρ: fluid density; two-dimensional [2D] vertical case relations), and the topological characteristics of recurring patterns.

The relevant studies are numerous, yet some of them are of specific importance for the present investigation. Namely, Nadaoka et al. (1989) used Laser Doppler Velocimetry (LDV) for flow visualizations and Eulerian velocity measurements to indicate that characteristic large-scale eddy structures under breaking waves transform from 2D structures with horizontal axes parallel to the crest line to three-dimensional (3D) obliquely descending eddies (ODEs) behind the wave crest. Emerging vortical patterns, traced at the breaking wave front, were finally entrained through large-scale eddies into the underlying flow field. The separation of the irrotational velocity components (ordered wave motion) from the rotational mean velocity (eddy motion) was achieved through filtered phase-averaging of the velocity field. The generation of the vorticity field, related to the mean velocity component, caused considerable increase in mass and momentum transport and affected the wave height evolution in the surf zone. Cox and Kobayashi (2000) attempted LDV measurements of instantaneous values of u', w', τ_{ss} and k. They also traced coherent structures, yet through simple phase-averaging. Moreover, quadrant analysis of u' and w' helped them define coherent motions, and conditional sampling techniques defined the statistics of coherent and intense events of intermittent nature. They concluded that the dominant vortices are of micro- or mid-size and of small life-span, yet carry up to nearly 50% of the total turbulent energy under the wave crest.

Stansby and Feng (2005) used a large number of gauges, in order to investigate thoroughly the kinematics of the surf zone created by weakly plunging breaking waves. Through ensemble-averaging (Nadaoka et al., 1989), they determined the recurrent flow structures on a vertical 2D plane, including from large-scale motions down to small-scale vortical structures. Multiple coherent structures at the onset of breaking transformed to elongated structures near and along the free surface during the bore propagation. Period-averaged ω, u and w were also obtained showing breaker-induced onshore mass transport above trough level against the undertow below it, while thick vorticity layers were traced at trough level and thin counter-rotating ones near the bed.

On the other hand the Large Eddy Simulation (LES) approach discerns nowadays in numerical modelling of wave breaking turbulence. Relevant applications are numerous, yet some of them are referenced concisely, as important in the present study. Christensen and Deigaard (2001) used a sub-grid scale Smagorinsky-type model for the unresolved flow scales and depicted complicated flow phenomena such as ODEs. Christensen (2006) implemented LES to calculate the wave set-up, the undertow and turbulence features, yet for a rather coarse computational resolution, thus an overall overprediction of turbulence levels was found. Except from mesh-based LES methods, Smoothed Particle Hydrodynamics (SPH) is widespread nowadays in the numerical modelling of free surface flows. Nevertheless, visually impressive SPH wave breaking simulations (Gómez-Gesteira et al., 2010b) somehow lack thorough affirmation concerning turbulent flow features. Shao and Ji (2006) proposed a LES-type SPH approach by using a Sub-Particle Scale (SPS) turbulence closure model. Results were good only in terms of η, u', and w'. Very recently, Farahani and Dalrymple (2014) studied the turbulent vortical structures under spilling breaking of solitary waves with the use of 3D SPH. Their numerical results compared very well against experimental data in terms of water surface evolution and horizontal velocities. They detected coherent structures, organized in space and time, in the form of reversed horseshoe (hairpin) vortices submersing downward behind the spilling breaker. These structures were related to sweep events of turbulence that transported momentum and TKE towards the bed, through a downwelling motion, with a clear vortex turning mechanism. Similar coherent flow patterns were not detected for the case of a plunging solitary wave breaker. In trying to fill the gap we hereby implement state-of-the-art SPH for wave breaking in weak plunging form.

2. METHODOLOGY

2.1 SPH model

SPH method (Monaghan, 2005) is one of the most ingenuous modern numerical methods for the simulation of hydrodynamic free surface flows (FSFs). It is a mesh-free particle method, implementing Lagrange-type notation for Navier-Stokes equations, through integral interpolation smoothing functions. Its Lagrangian nature allows the unhindered simulation of FSFs with strong deformations, such as wave breaking (e.g. plunging) in coastal areas, as described by Dalrymple and Rogers (2006). Thorough analysis of SPH can be found in the book of Violeau (2012), thus only general reference of the constitutive equations and assumptions used is given here. Hence, the method's fundamental principle is the integral interpolation of any given (scalar or vectorial) function $A(\mathbf{r})$ and/or its derivative in the computational domain that reads in analytical form and gives rise to the discretized notation for the function A and its derivative, as:

$$A(\mathbf{r}) = \int A_j(\mathbf{r}')W(\mathbf{r}-\mathbf{r}',h)d\mathbf{r}' \;\Rightarrow\; A_i(\mathbf{r}) = \sum_j A_j(m_j/\rho_j)W_{ij} \;\Rightarrow\; \nabla A_i = \sum_j A_j(m_j/\rho_j)\nabla_i W_{ij} \qquad [1]$$

where $h=c_f[(dx)^2+(dz)^2]^{1/2}$ is the smoothing length in 2D, dx and dz is the horizontal and vertical spatial discretization respectively, c_f is a smoothing calibration parameter, $\mathbf{r}$ and $\mathbf{r}'$ are the arbitrary particle location and the distance between particles respectively, $W(\mathbf{r},h)$ is the distance-varied weighting function called "kernel", i corresponds to an arbitrary particle (center of SPH interpolations) and j to particles within the compact support region of the kernel for particle i, m_j and ρ_j are the mass and density of particle j; W_{ij} is the kernel in particle notation. In order to verify the capability of state-of-the-art SPH to predict the details of the entire wave breaking process, the academic 'open source' numerical code SPHysics v.2 (Gómez-Gesteira et al., 2010a; 2010b) was used. The solid walls of the computational domain were treated as repulsive, which defined a more or less slip boundary condition at the inviscid limit (Gómez-Gesteira et al., 2010b). The symplectic time-integration technique with variable time step (Gómez-Gesteira et al., 2010a) was preferred for fastness. Similarly to LES, the SPS approach (Appendix of Gómez-Gesteira et al., 2010a) was incorporated accounting for internal friction effects in terms of the stress tensor (in Einstein notation):

$$\tau_{ij} = \overline{\rho}\left(2\nu_t \tilde{S}_{ij} - 2\left(\nu_t k_{SPS}\delta_{ij} + C_I \Delta l^2 \delta_{ij}\left|\tilde{S}_{ij}\right|^2\right)\big/3 \right) , \; \nu_t = \left[\min(C_s \Delta l)\right]^2 \left|\tilde{S}_{ij}\right| \qquad [2]$$

where ν_t is the turbulent eddy viscosity, $C_I=0.0066$, Δl is the inter-particle spacing, δ_{ij} is the Kronecker delta, k_{SPS} is the SPS TKE, $|\tilde{S}_{ij}|$ is the local strain rate calculated from the resolved variables, i.e. the norm of the second-order invariant of the Favre-filtered strain rate tensor. The eddy viscosity assumption (Boussinesq approximation) was employed in the framework of a standard, non-dynamic Smagorinsky model with a constant coefficient $C_s=0.145$ both in space and time.

2.2 Computational setup and experimental data

The experimental data, adopted for the validation of SPH simulations, were collected from the physical modelling study of weak plunging breakers and consequent turbulence transport under them, by Stansby and Feng (2005) [SF05 hereafter]. A sketch of the flume setup is presented in Fig. 1 (left). The geometric and hydraulic features of the experiment can be found in SF05 and Makris et al. (2011; 2012; 2014). It was found that in the initial breaking phase, a cluster of nearly horizontal eddies (rotation axis parallel to the shore) was formed in the water column. Thereafter the weak plunging jet re-splashed several times and generated patterns of recurring coherent vortical structures, leading to the formation of a series of horizontally elongated eddies above trough level and near the free surface. The numerical wave tank of the vertically 2D SPH simulations was directly correspondent to the experimental one; all SF05 results were presented on a vertical cross-section in the middle of the laboratory wave flume. In particular, measurements of all hydrodynamic features

were conducted at discrete numerical gauges in respect to the record locations of SF05. The horizontal distances x_g of crucial gauges from the wavemaker are given in Table 1, together with the local depth *d*. In brief, gauges G8 and G10 were placed in the incipient breaking region of the plunger, whereas G21 and G23 corresponded to the inner surf zone. To sample the scattered (Lagrange-type) SPH fluid data A_p on fixed (Eulerian) nodal points A_n, a convenient interpolation method was used, based on the spatial averaging notion by Farahani et al. (2012), i.e. a convolution integral for particles:

$$A_n = \sum_{p=1}^{N} A_p \left(m_p / \rho_p \right) W \left(\left| r_n - r_p \right|, h \right) \qquad [3]$$

where *p* is any neighbour particle in an area of radius r_p, around the fixed computational node *n* that corresponds to the exact position of the Eulerian numerical gauge and *N* is the total number of particles that satisfy the relation $r_p \leq h$. We hereby imposed this interpolation technique, but only at the column of vertically discretized nodes *n* that correspond to the Eulerian numerical gauge and not over the whole computational domain, in order to avoid increase of computational time.

The accurate discrimination of the rotational wave components of motion from fluctuating ones is a formidable task in wave breaking (Nadaoka et al., 1989), because the irregular velocity components relate to either turbulence or the rotational motions of the wave and are superimposed reciprocally in several bands of the Fourier spectrum. Coherent structures reside somewhere in between, and part of them is of small scale and high frequency. Thus a simple phase-averaging operator e.g. for the velocity field ‹**u**› (Ting and Kirby, 1995) under breaking waves is not sufficient, in order to extract properly the ordered wave motion from the raw velocity **u** data, because the latter contain irregularly fluctuating components of both coherent structures and residual fluctuating motions. In order to decontaminate the numerically recorded signals, we followed SF05 and implemented the ensemble-averaging method of Nadaoka et al. (1989). It comprises of a low-pass filter on the raw data, to remove residual turbulent components, and subsequent phase-averaging for several cycles of the low-pass filtered values of flow features, e.g. for the velocity field, given by:

$$\mathbf{u}_{ens}\left(\mathbf{x}, \zeta t\right) \equiv \left\langle \tilde{\mathbf{u}}\left(\mathbf{x}, \zeta t\right) \right\rangle = \frac{1}{N} \sum_{i=0}^{N-1} \tilde{\mathbf{u}}\left(\mathbf{x}, \zeta\left(t + iT\right)\right) \qquad [4]$$

where ‹•› is the phase-average operator, the tilde sign (~) denotes filtered values by the moving average technique, *i* is the sample indicator, *N* is the maximum sample number equal to the simulated wave cycles, *T* is the wave period, ζ is the wave angular frequency, **x** is the position vector and *t* is the time interval of computations.
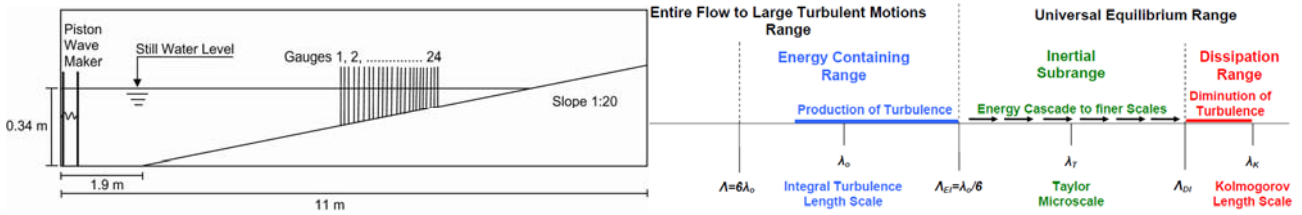

Figure 1. Sketch of the SF05 experimental/computational setup (left). Diagram of turbulent flow length scales and eddy sizes (right).

2.3 Analysis of flow scales and model resolution

Before defining the particle discretization Δx of the SPH simulation, analysis of the real flow scales should shed some light on SPS-SPH model's potential to perform satisfactorily as a pseudo-LES approach. The length scales of turbulent motions could be divided into three categories, as depicted in Figure 1 (right diagram). The first one is the integral turbulence length scale λ_0, which corresponds to the energy containing range of the flow, which is relevant to large eddies containing a big part of coherent structures of the flow and corresponding to the largest wavenumbers of the turbulence energy spectrum (Pope, 2000). In this range, turbulence is produced, large velocity fluctuations are manifested, and high anisotropy is apparent. According to Cox et al. (1994) the mixing length is related to turbulent length scales λ_0 as:

$$\lambda_0 = \kappa \left(z - z_0 \right), \textit{ for } z < z_{cr} \quad or \quad \lambda_0 = C_\lambda d, \textit{ for } z \geq z_{cr} \qquad [5]$$

where κ is the Von Karman constant ($\kappa \approx 0.4$), z_0 is the bottom elevation, *z* is the vertical distance, $z_{cr}=(C_\lambda d/\kappa)+z_0$ is a critical value determining the bottom boundary layer, and C_λ is a time-invariant empirical coefficient. For the case of intensely spilling breaking waves, Cox et al. (1994) calculated overall values of C_λ to be 0.04 at the incipient breaking region and 0.18 in the inner surf zone. The upper limit of the integral turbulence length scales is $\Lambda=6 \cdot \lambda_0$ (Pope, 2000), and was calculated to vary from 25% to 100% of *d*, from the vicinity of the breaking point to the inner surf zone respectively. The lower limit is $\Lambda_{EI}=\lambda_0/6$ and sets the demarcation point between the anisotropic large eddies, $\lambda > \Lambda_{EI}$, and the isotropic small eddies, $\lambda < \Lambda_{EI}$ (Pope, 2000). Its value was found to range from 0.7% to 3% of *d*, from the outer to the inner surf zone respectively. The calculated percentages refer to the water column outside the boundary layer ($z \geq z_{cr}$) for the specific hydraulic and geometric features of the experiment implemented (SF05). Based on Eq. [5], we derived the values of λ_0, Λ, Λ_{EI}, z_{cr} on crucial gauges of the numerical tank (Table 1). Λ_{EI} designates the boundary between λ_0 and the Taylor microscales λ_T. The latter correspond to the inertial subrange of turbulence, where energy cascades to finer length scales without dissipation. Their lower limit is Λ_{DI} and discriminates them from the smallest length scales in the spectrum, namely the Kolmogorov scales λ_K, for which energy is dissipated due to viscosity. According to Table 1, values of integral turbulence length scales λ_0 range from 5.9 to 6.3 mm in the outer surf zone and from 1.35 to 1.71 cm in the inner surf zone, for the water column outside the bottom boundary layer ($z \geq z_{cr}$). The depth-averaged corresponding values for $z < z_{cr}$ were half the latter (minimum $\lambda_0 = \sim 3$ mm) throughout the entire surf zone. The initial particle resolution Δx should have sufficiently smaller values than calculated λ_0 throughout the entire computational domain, in order to render the SPS model effective in reproducing large-scale coherent structures of e.g. vorticity. Moreover, Λ_{EI} is everywhere smaller than 3 mm, and reaches a low of 1 mm for $z \geq z_{cr}$ and 0.5 mm in the middle of the bottom boundary layer. Based on that

observation, the finest case we could simulate, with a serial code like SPHysics v.2, was with a spatial resolution of $\Delta x=\min(\Lambda_{EI})=1$ mm for $z{\geq}z_{cr}$, even marginally meeting the demands of $\Delta x<\Lambda_{EI}$ inside the bed boundary layer only at the inner surf zone. Our simulations engaged nearly 1.8 million particles, and it took nearly six months for the completion of a single run! Thus in the present study, the 2D turbulence for all scales, below either λ_0 or Λ_{EI} in most areas of the domain, was computed with a Smagorinsky-type SPS model. Please note that there is still a long way for a complete LES implementation in our SPH analysis, e.g. explicitly simulating at least 80% of the 3D flow, moving towards and beyond Taylor microscales. The latter implies implementing hundreds of millions of SPH particles and massively parallel simulations, even for such a scaled down geometry. Our simulations involved 10 to 50 wave periods, to ensure that sufficient data would be obtained in order to conduct analysis of intermittent features and their statistics (Cox et al., 1994). The initial time step was $\Delta t=1.5 \cdot 10^{-5}$ sec, and the sampling rate of numerical output was 100 Hz (Cox et al., 1994), thus recording nearly every 600 time steps. This meant 242 records of hydrodynamic features per T and $1.21 \cdot 10^4$ per run.

Table 1. Integral turbulent length scales λ_0, with upper and lower limits Λ and Λ_{EI}, at specific gauges (d: depth; x_g: gauge positions from the wavemaker) for the water column above the boundary layer threshold ($z \geq z_{cr}$) and in the middle of the boundary layer ($z < z_{cr}$).

Gauge	x_g (m)	d (m)	z_{cr} (m)	$z \geq z_{cr}$			$z < z_{cr}$		
				Λ (m)	λ_0 (m)	Λ_{EI} (m)	Λ (m)	λ_0 (m)	Λ_{EI} (m)
G8	5.540	0.1580	0.0158	0.0379	0.0063	0.0011	0.0190	0.0032	0.0005
G10	5.737	0.1482	0.0148	0.0356	0.0059	0.0010	0.0178	0.0030	0.0005
G21	6.796	0.0952	0.0472	0.1028	0.0171	0.0029	0.0566	0.0094	0.0016
G23	7.200	0.0750	0.0359	0.0810	0.0135	0.0023	0.0431	0.0072	0.0012

3. SPH MODEL EVALUATION

We validated the SPHysics v.2 model based on comparisons of simulations' results against experimental data (SF05) for several wave characteristics and their evolution in the cross-shore direction, covering the whole computational domain. Comparisons are very good in terms of wave heights and free surface elevations and somewhat acceptable for velocities.

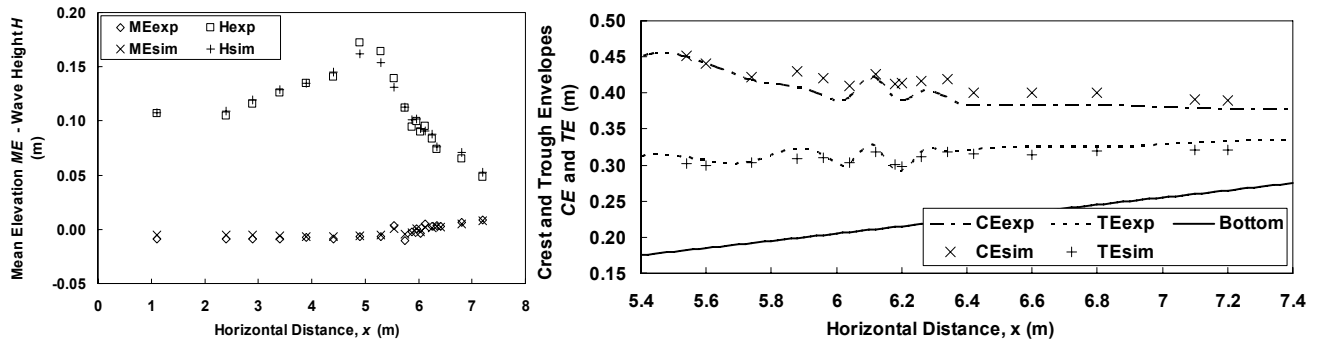### 3.1 Wave heights, set-up, crest and trough elevation

Figure 2. Wave height H, mean free surface elevation ME (left graph); Crest and trough envelopes, CE and TE, respectively (right graph). Comparisons between experimental data (exp) and simulations' output (sim).

The wave heights H were computed at every gauge with the use of a zero-upcrossing technique. The values of H were averaged for up to 50 wave cycles excluding measurements for the first three wave periods, which were considered to constitute a reasonable warm-up period. In Figure 2 (left graph) the comparisons of experimental against numerical wave heights H and wave set-up (wave-induced, mean, free surface elevation) ME are shown. The wave breaking point was very well predicted, the trend of wave height evolution was plausibly reproduced and simulated values of H revealed insignificant deviations from experimental ones. Minor discrepancies are depicted in the shear-intensified region of the plunging event. Furthermore, the wave set-up ME was impressively predicted throughout the entire computational domain, which is hard to achieve with the use of classic wave models. The Pearson product-moment correlation for the wave height distributions by simulations against experiments was larger than 0.96. In the wave propagation and shoaling regions or in the turbulent bore region and the inner surf zone, even simulations with rather coarse spatial resolution could yield good results (Makris et al., 2011; 2012). Comparisons of wave crest and trough envelopes (CE and TE) are also presented in Figure 2 (right graph) between numerical simulations and experiments, covering the entire surf zone. Please note that the CE and TE represent the marginally higher and lower values of the free surface elevation η for the passing of all waves. Agreement is acceptable especially for the trough level even in the shear intensified region of initial breaking.

3.2 Ensemble-averaged and root-mean-square wave features

The heuristic approach to analyze the flow field structure under breaking waves, rendered by Nadaoka et al. (1989), was used in the present study to define the ensemble-averaged values of several wave features (see Section 2.2). The method actually consisted of applying an explicit low-pass filter on the record signals obtained from the numerical gauges. Hence, an attempt was made to reduce the contamination by the lower-frequency effects of the rotational wave components with the use of a moving-average method, where each wave cycle was divided into time-blocks. Velocities, free surface elevation, etc, were averaged for each segment of the signal. Subsequently the phase-averaging operator of Eq. [4] was applied to each corresponding time-block, over all wave cycles of the simulation, in order to derive the aggregate mean

cyclic variation (SF05). The amount of time-segments is relevant to the hydrodynamic features of interest. In the present study the large scale motions, the recurring vortical patterns, and the coherent structures were of major importance. Following SF05, 121 time-blocks were implemented, which corresponded to a moving average time of 0.02 sec (frequency of 50 Hz) and gave 3 samples per time-block for the sampling rate of 100 Hz. The Nyquist limit, i.e. the cut-off frequency in order to fully reconstruct the initial signal or resolve the coherent structures with residual superimposed random fluctuations (SF05), was 25 Hz. This value corresponded to nearly 60 times the wave frequency f_w (60th harmonic). In Figure 3 (upper graphs) comparisons of ensemble-averaged values of free surface elevation η_{ens} between experimental data and SPH simulations are presented, at specific gauges in the incipient breaking region and the inner surf zone; the best-fit distribution of raw η in one wave period T=2.42 sec (x-axis) is also given indicatively. Very good agreement was found covering the entire surf zone. Similar comparisons are shown in the lower graphs (Figure 3) for the ensemble-averaged values of depth-averaged velocity U_{ens}. Results continue to be good at the inner surf zone, yet simulated U_{ens} was somehow underestimated at the shear intensified regions, probably due to lack of robust treatment for bottom friction and boundary layer kinematics in SPH simulations. Spatial resolution down to Taylor micro-scales ($\Delta x < \Lambda_{El}$) should be considered in the future. Nevertheless, the respective raw values of U for an arbitrary wave cycle were very close to the ensemble-averaged experimental data. In Figure 4 (left graph) the root-mean-square (rms) values of the fluctuating free surface elevation $\eta_f = \eta_{ens} - \eta_{mean}$ (η_{mean} is the period-averaged η), are given at all the gauges of the surf zone. Comparisons with experimental values revealed exquisite agreement (Pearson correlation coefficient very close to unity). This was not the case though for the rms depth-averaged velocity U_{rms} (Figure 4; right graph). Correlation coefficient was about 0.5, which is somewhat dissatisfying. Nonetheless, the latter applied mostly along the transition region of the plunger to a bore in the mid surf zone. At the incipient breaking region or the inner surf zone comparisons with experimental data were acceptable. However, the SPS-SPH model provided apparently far better results than the RANS model of SF05.
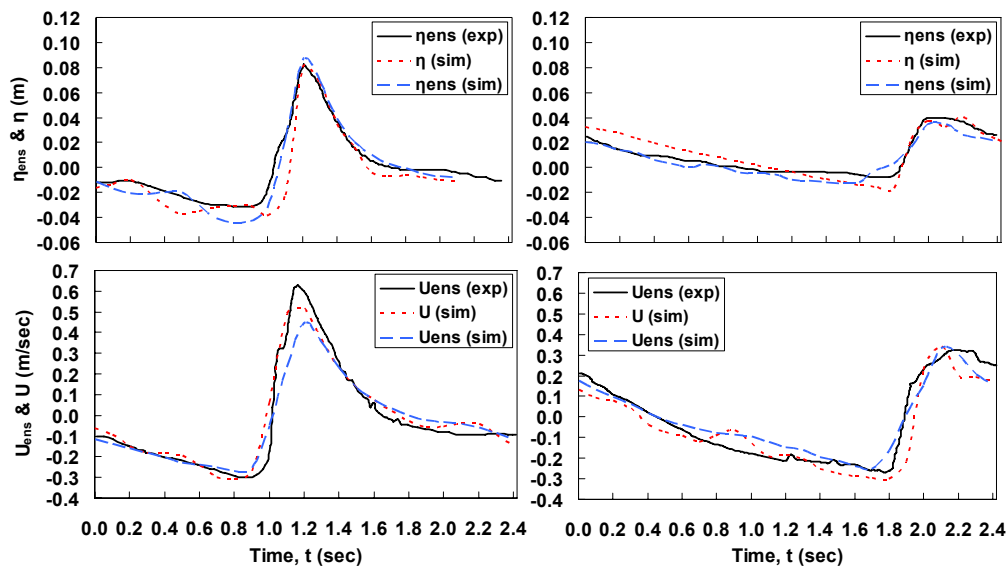

Figure 3. Ensemble-averaged (blue/long-dash line) and real-time (red/short-dash line) values of free surface elevation (upper graphs), η_{ens} and η, and depth-averaged velocities U_{ens} and U (lower graphs). Left graphs refer to incipient breaking region (G10) and right graphs to the inner surf zone (G23). Comparisons between experimental data (exp; solid black lines) and simulations' output (sim).
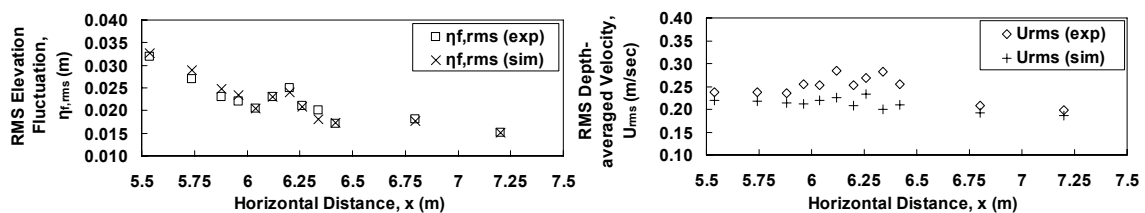

Figure 4. Comparisons of experimental (exp) against simulated (sim) rms values of free surface elevation fluctuation $\eta_{f,rms}$ (left graph) and depth-averaged velocity U (right graph).

4.   SPH RESULTS IN THE SURF ZONE OF WEAK PLUNGERS

We have shown in the past (Makris et al. 2011; 2012) good representations of weak plunging breakers with the SPHysics v.2 model for rather fine particle resolutions (Δx=3 mm). The characteristic jet with the consequent rebound on the forward trough of the wave, was well reproduced. In the following, various numerical results are presented, based on the validated SPH simulations, ranging from wave-induced currents to features of 2D dynamics, which capture the majority of the cross-shore phenomena in the entire surf zone and provide significant insight on the fluctuating hydrodynamic components.

4.1   Wave-induced mean flows

The investigation of surf zone hydrodynamics in this study focused on the simulation of the cross-shore, seaward, return flow (undertow) and the shoreward flow above the trough level (broken wave mass transport added to the Stokes drift). In Figure 5 (upper graph) the Eulerian period-averaged kinematics at specific gauges in the surf zone are portrayed. The

onshore current comprises the Stokes drift together with the broken wave's net mass transport, while the undertow is the counterflow below. These opposite wave-induced currents are clearly discerned by the calculated wave trough and crest envelopes. The wave set-up level was plausibly positioned between them realistically depicting the propagating wave's advancing nonlinearity. Figure 5 reveals qualitative similarities when compared to the respective representation by SF05. Moreover, even the shoreward inversion of the mean flow near the bed, called "streaming" (Longuet-Higgins, 1953), was reproduced. The latter is shown by the onshore vectors of mean velocity on the bottom boundary. This is in fact the time-average of the wave-induced oscillatory motion, which could influence significantly the shear stress vertical distribution in the boundary layer. As an outcome, coherent structures of rotation emerged near the bed, observed in following ω maps.
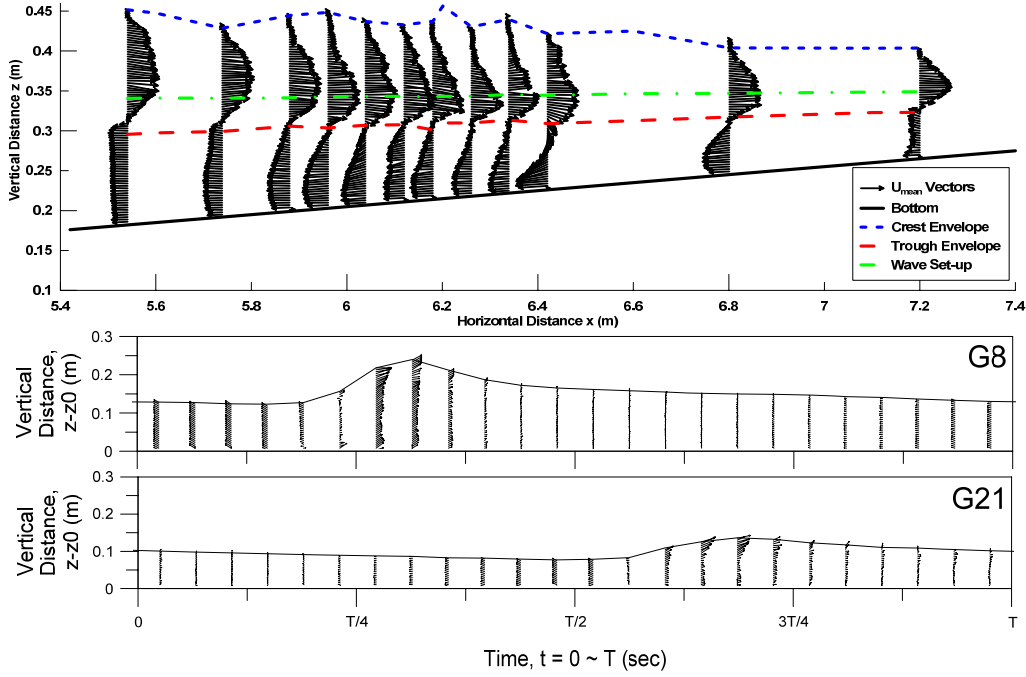

Figure 5. Period-averaged vertical distribution of velocity vectors at various gauges in the surf zone (upper graph). Wave trough (red large-dash line), crest (blue small-dash line) and set-up (green dash-dot line) envelopes are shown, demarcating the undertow and shoreward drift regions. Ensemble-averaged velocity vector plots at the outer (G8) and inner surf zone (G21).

Plots of simulated ensemble-averaged velocity vectors $\mathbf{u}_{ens}$ are also shown in Figure 5 for the weak plunging breakpoint (middle graph; G8) and the propagating bore (lower graph; G21). Please note that the plots are against time for a whole wave period T. It was found that the velocity magnitudes were similar to measured wave celerity c, in the roller and bore regions. The highest values were observed during the initiation of plunging breaking, as water jets were formed and crests overturned; the lowest values were in the vicinity of the turbulent bores, probably due to their diffusive nature (SF05). The maximum velocity occurred at the wave crest above the toe of the wave in the incipient breaking region (G8) with magnitudes almost $1.5 \cdot c$. At G21 (inner surf zone), the maximum values of numerically derived $\mathbf{u}_{ens}$ were 7% to 12.5% higher than c. It is obvious that the vertical distribution of $\mathbf{u}_{ens}$ vectors was of oscillatory nature, i.e. with counterbalancing direction, during one wave cycle (Figure 5; middle and lower graphs), similarly to Nadaoka et al. (1989). Gradients in velocity distributions could be associated to the 2D coherent shear and vortical structures shown further below. Nonetheless the effect of boundary layer vorticity to the simulated velocity was not as important as that due to the large-scale eddies above trough level, because the bed roughness was negligibly small in the present study (SF05). Furthermore, in order to check the counterbalancing effect of the undertow and the shoreward drift, the period- and depth-integrated values of ensemble-averaged and mean velocities' vertical distributions were calculated by the relations:

$$Flux\left(\mathbf{u}_{ens}\right) = \int_0^T \int_{z_0}^{\eta} \left(\mathbf{u}_{ens}\right) dz dt \; , \quad Flux\left(\mathbf{u}_{mean}\right) = \int_{z_0}^{\eta} \left(\mathbf{u}_{mean}\right) dz \qquad [6]$$

Eq. [6] actually describes the 2D volume fluxes of period- and ensemble-averaged velocities, which are far less than 0.01 m²/sec, i.e. practically almost zero in all gauges. The naught balance in shoreward and offshore driven momentum, indicated plausible qualitative reproduction of the wave-induced mean flows throughout the surf zone. No need of any special treatment for the vertical distributions of the velocity field emerged for the SPH model.

4.2 Spectral analysis of fluctuating velocity components

The SPS-SPH model implemented hereby, similarly to LES-type approaches, is very close to experimental investigations in regard to the issue of distinguishing the fluctuations of the hydrodynamic field from the regular or ordered water motion (Christensen and Deigaard, 2001). Thus an attempt was pursued to describe the overall, the residual and the intermediate fluctuating point-measured velocities, u', u'' and u''' respectively. The latter were computed by appropriate operations involving the filtered and ensemble-averaged values, $\tilde{u}$ and $\langle \tilde{u} \rangle$, which were derived from raw velocities u produced by the 2D SPS-SPH simulations (Section 2.2). The three components of fluctuating quantities relate through superposition, according to the following:

$$\mathbf{u}'\left(\mathbf{x},\zeta t\right) = \mathbf{u}\left(\mathbf{x},\zeta t\right) - \left\langle \tilde{\mathbf{u}}\left(\mathbf{x},\zeta t\right)\right\rangle$$

$$\mathbf{u}''\left(\mathbf{x},\zeta t\right) = \mathbf{u}\left(\mathbf{x},\zeta t\right) - \tilde{\mathbf{u}}\left(\mathbf{x},\zeta t\right) \qquad \mathbf{u}'\left(\mathbf{x},\zeta t\right) = \mathbf{u}''\left(\mathbf{x},\zeta t\right) + \mathbf{u}'''\left(\mathbf{x},\zeta t\right) \qquad [7]$$

$$\mathbf{u}'''\left(\mathbf{x},\zeta t\right) = \tilde{\mathbf{u}}\left(\mathbf{x},\zeta t\right) - \left\langle \tilde{\mathbf{u}}\left(\mathbf{x},\zeta t\right)\right\rangle$$
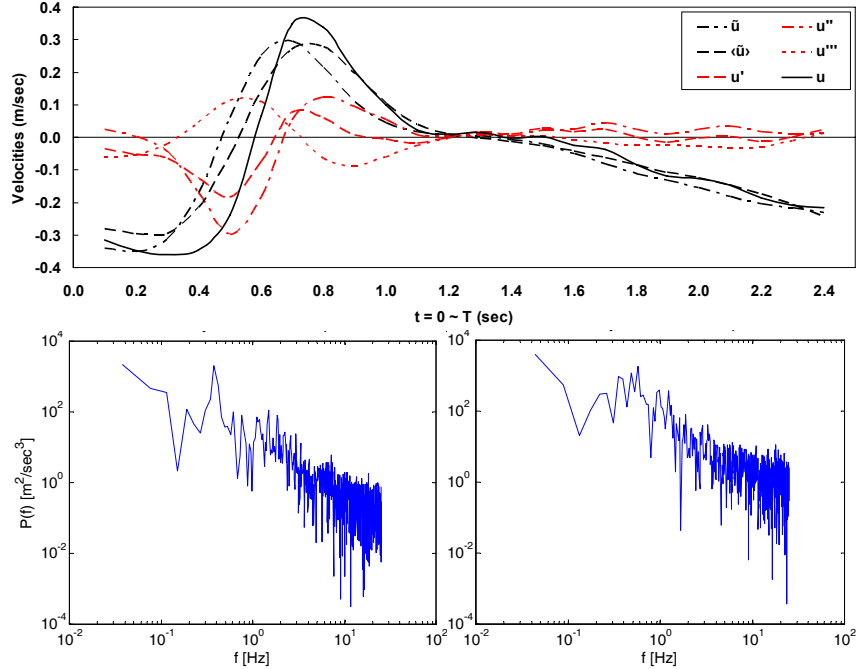

Figure 6. *Upper graph*: Simulated horizontal velocity u components of filtered $\tilde{u}$ and ensemble-averaged $\langle\tilde{u}\rangle$ values together with their fluctuating counterparts u', u'', and u''' representing the approximate turbulent intensities at the initial breaking point (G8). *Lower graphs*: Fourier spectra $P(f)$ of simulated fluctuating components for horizontal velocities u' at the incipient breaking region (G8) [left graph] and the inner surf zone (G23) [right graph]. Measurements are taken at still water level with the Nyquist frequency set at f_N=25 Hz.

In Figure 6 (upper graph) the signals of all fluctuating, filtered, averaged and raw velocities are presented for a single wave cycle. It is obvious that $\tilde{u}$ και $\langle\tilde{u}\rangle$ are smoothed out components of the SPH produced u on the numerical gauge, and that their remainder signals correspond to u'' and u'. The recorded u signal has its minimum values shoreward of the wave front, and reaches its maximum with the passing of the broken wave's crest until $t \approx T/2$. In the second half of the wave period, fluctuating intensities damp out suddenly. The u''' harmonic corresponds to a part of the large-scale coherent motions and has everywhere opposite sign from the residual and the overall components, u'' and u'. This means that the coherent structures tend to amplify the velocity u magnitude when it is smooth and on the contrary tend to restrain the positive exacerbations of the u signal. Furthermore, we attempted analysis of the spectrum for the overall fluctuating (approximate turbulent in 2D) components of the horizontal (Eulerian) velocity field u', shown in the lower graphs of Figure 6 for the outer and the inner surf zone. This was achieved through discrimination of the ensemble-averaged components u_{ens} (Eq. [4]) from the raw velocities u, obtained by high sampling rate numerical records, following the first relation of Eq. [7]. The Fourier power-law spectra $P(f)$ (f is the frequency) followed a trend of -5/3 gradient on the log/log scale, which is typical of isotropic (inertial sub-range) turbulence (Pope, 2000). This trend extended from f=1 Hz up to the Nyquist filter limit f_N=25 Hz. Random turbulence below this frequency was lost in the averaging process. Consequently the lower limit of the large-scale structures' life-span t_{cs} would practically be of the $O(t_{cs})$=1 sec, while approximate turbulent energy cascade would involve coherent structures with t_{cs} at most of the $O(t_{cs})$=0.04 sec. Improvement of previous results on the matter, based on lower spatial resolution (Makris et al., 2011; 2012), was clear for median to high frequency bands that correspond to either the SPS-treated length scales or the smallest of the resolved large motions. In the present study the finer spatial resolution and sampling, together with sufficient number of cycles simulated, contribute positively to the upgrade of numerical results. Nevertheless issues of proper treatment for turbulence measurements still remain, since the -3 gradient, typical of 2D frozen turbulence (Pope, 2000), was not reached anywhere in the computational domain. All the above were relevant to areas inside the surf zone near the still water level, where thick layers of vorticity and strong vorticity gradients were present. Throughout the rest of the water column, the spectra revealed anisotropic trends for even broader frequency band widths, namely for larger scale (coherent) structures in the flow field.

4.3   Coherent vortical structures

We also studied the reproduction of Lagrangian and Eulerian recurring patterns of vorticity ω and respective coherent structures. For a 2D vertical plane of the hydrodynamic field, ω is always perpendicular to the flow and could be considered as a scalar field, given by $\omega = \partial u/\partial z - \partial w/\partial x$. In Figure 7 (lower graphs) three characteristic snapshots of the ω field are shown. Vorticity started to gain noticeable values at the wave crest and the toe of the wavefront right before the plunging jet formation, as in Zhao et al. (2004). Concentrated vorticity spread out over the whole surface roller region with the initiation of the plunging breaking process. Subsequently, the impingement of the plunger on the forward trough induced the generation of topological vorticity independent of the wave-induced rotational flow. A sudden burst of vorticity took place and confined multiple vortical structures became apparent. A small part of them was descending obliquely to

the bottom spreading also vorticity in the water column for a brief period after plunging. The larger part of them was permeated near the free surface, seaward of the broken wave crest. This might be considered as the end of the plunging region and the start of bore propagation. During the latter coherent vortical structures were initially stretched horizontally, just as reported by SF05. Eventually they were convected vertically along the entire water column, resulting in the formation of discrete large coherent structures in the bore region. Everywhere else the flow was nearly irrotational, except in the region upstream of the plunger, where short coherent structures and torpid residual vorticity of low values was observed, due to the passage of previous breakers. We also observed the formation of a thin layer of negative vorticity (counter-clockwise rotations) that prevailed at the bottom. These persisting elongated structures were observed near the bed under and in front of the roller, initially similar to a mixing layer, just as shown by SF05 and Nadaoka et al. (1989). These and the formerly mentioned coherent structures in the roller region are most important in bed sediment pickup and suspension respectively. All the aforementioned patterns of ω appeared periodically (coherent structures) with every other wave. We also plotted the simulated period-averaged ω field, presented in Figure 7 (upper graph) for the surf zone. The axes are distorted, thus the actual structures are much more elongated than those presented. A thick layer of mean clockwise vorticity was traced in the vicinity of the wave trough level at the end of the initial breaking region, as reported also in SF05. A successive pattern of positive and negative concentrated vorticity was apparent at trough level in the bore region, followed by counter-rotative structures near the bed. The horizontal length scale of the period-averaged coherent vortical structures, contained in the two aforementioned discrete regions, were 22% to 24% of the local wave length (L_{vort}=22~24%·L) or 4.5 to 6.5 times the local water depth (L_{vort}=4.5~6.5·d).
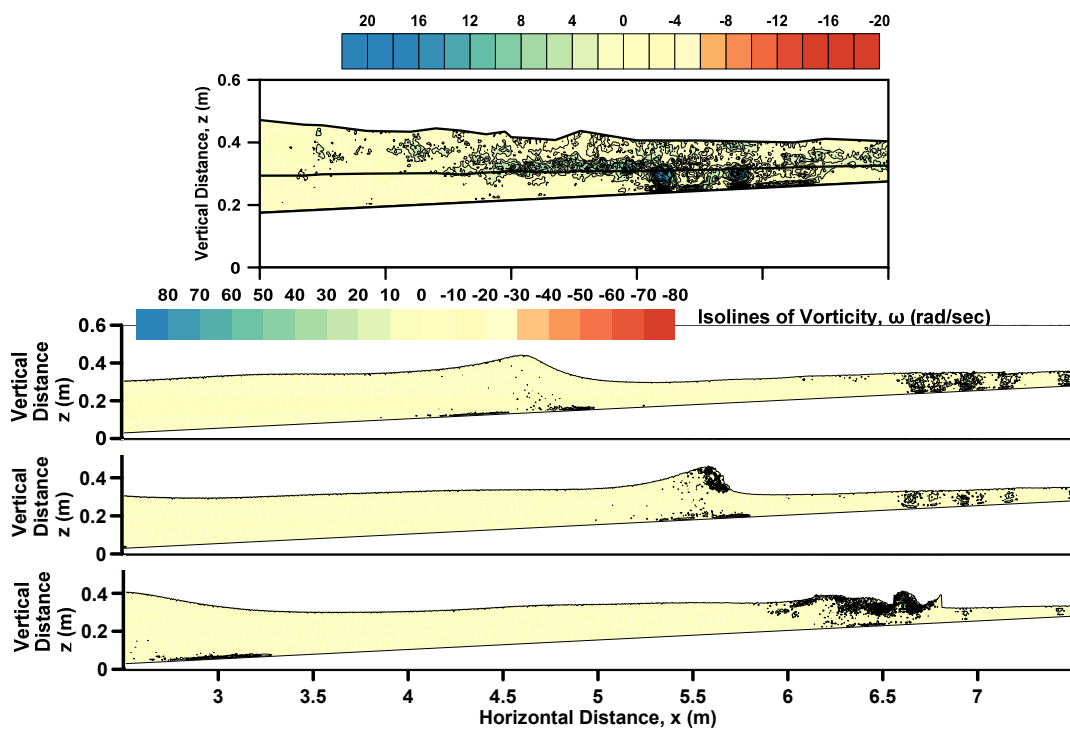

Figure 7. Simulated coherent structures of the period-averaged (upper graph) and the instantaneous (3 lower graphs) vorticity field ω (sec^{-1}) under weak plunging breaking waves. In upper graph the full lines show crest and trough trajectories and bottom elevation.

Simulated ensemble-averaged vorticity ω_{ens} contour plots are shown in Figure 8 (left graphs: incipient breaking region; right graphs: inner surf zone). They refer to numerical measurements of the vertical distribution of $\omega_{ens}(z)$ and its evolution in time at discrete fixed (Eulerian) gauges (method in Section 2.2). Concentrated vorticity was apparent as multiple coherent structures at the initial breaker point (G8), the surface roller (G10) and the bore (G21, G23) region. In the latter, those structures were spread mainly horizontally. They formed a recurring pattern and could be characterized as coherent by taking into account that $\omega(z)$ has been ensemble-averaged for up to 50 wave cycles. In particular, vorticity was generated during the initiation of breaking (G8, G10), where positive values of (clockwise) ω_{ens} were traced near the crest and negative values of (anticlockwise) ω_{ens} near the bottom below the crest. These structures seemed to have a lifespan of t_{cs}=T/8≈0.3 sec. This corresponded to 30 record and 15 reconstructing values of the signal, enough for establishing coherence. In the inner surf zone (G21, G23) vorticity patterns were enfeebled yet still multiple in numbers, with the area around and above the trough being saturated by coherent structures. These were distributed along the surface as the bore propagated to shallower water in the swash zone. Initially (G8, G10) the maximum ensemble-averaged vorticity was about $\omega_{ens,max}$=33 sec^{-1} at the toe of the breaker, and rapidly reduced to about 50 sec^{-1} for downstream bores (G21, G23). Apart from the bore crest, small coherent structures were also present in the initial stages of the mean cyclic variations, i.e. for t=0~T/4, as residual vorticity upstream of the incident plunger due to the passage of previous breaking waves. Eventually the maximum recorded numerical vorticity was traced just before the coherent structures spread along the surface (SF05).

4.4 Coherent structures of TKE and Reynolds stresses

Another interesting issue, concerning the investigation of coherent structures derived from the fluctuating components of hydrodynamic features in the present study, was the derivation of the approximate TKE and Reynolds stresses on the 2D vertical plane. They were only calculated at fixed numerical gauges for the whole water column, and ensemble-averaged

over all wave cycles, in order to associate with the large coherent 2D vertical cross-sections of the actual eddies. Due to the neglect of the transverse horizontal velocity fluctuations v', the computed values of k were multiplied by a factor of ~1.4, i.e. a value in between the spilling (Ting and Kirby, 1995) and strong plunging cases (Christensen, 2006). Contour plots of k_{ens} on a 2D vertical cross-section are shown in Figure 9 (left graphs) for weak plunging breaking waves at fixed points in the incipient breaking region (G8) and inner surf zone (G21). This figure actually illustrates the temporal evolution of approximate turbulence production and decay in 2D, during the breaking process for a wave period, averaged over many cycles. 2D TKE was produced just before breaking at the toe of the roller and took higher values on the forward front and near the crest of the wave during plunging. The layers of k_{ens} were thin but very dense in the initial phase of the wave passage from the gauge. Afterwards, k_{ens} was diffused with time, especially when the back face of the wave was passing, thus rendering those layers sparser, thicker and of lower energy. In the incipient breaking region there were also very small values of TKE in the area below the wave trough and near the bed. TKE was obviously convected during the wave transition from a plunger (G8) to a bore (G21), revealing fast dissipation within one wave period (Zhao et al., 2004). A rapid downward reduction of TKE was obvious, probably due to the domination of fluctuations' transport over production below the trough (Ting and Kirby, 1995). Thus, unlike vorticity, no considerable amount of TKE remained behind as the wave moved into the surf zone. Therefore there were areas in the surf zone where TKE and ω were not correlated. Specifically during initial breaking (G8), TKE coherent structures were present in the roller region near the crest, whereas coherent vortical patterns were absent there. The same patterns were also observed at the bore region (G21). This means that there were considerable amounts of turbulence produced by the plunging jet without the creation of coherent vortical structures, and the residual vorticity after the passage of the wave was not accompanied by turbulence generation or conservation. Nevertheless, we should take into account that TKE calculated in the present study was only in reference to the low spectral frequency motions and not due to SPS flow. The TKE maxima of the simulated weak plunger were 0.57 to 0.21 $m^2 sec^{-2}$ from the incipient breaking region to the inner surf zone, hence the maxima of approximate turbulent intensities were equal to 63% and 53% of the overall energy for the initial and inner surf zone, respectively.
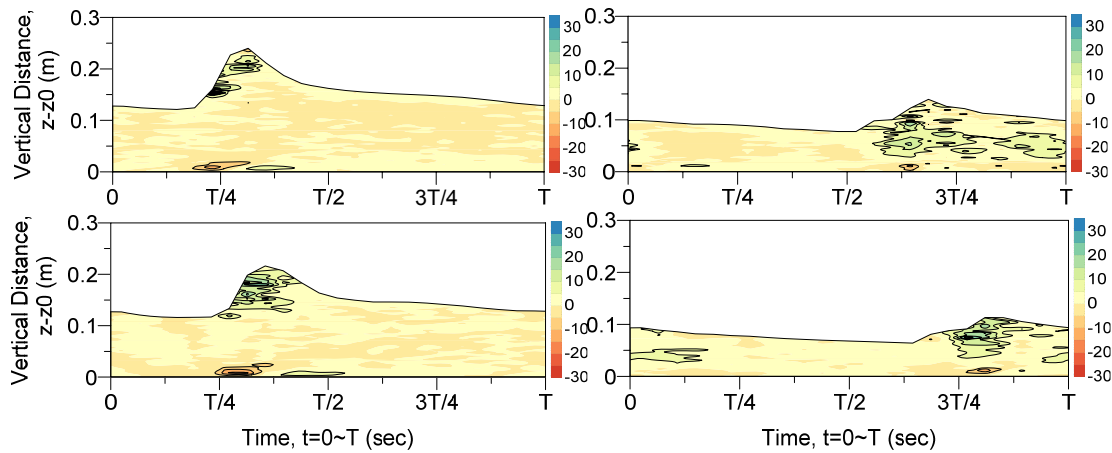

Figure 8. Simulated ensemble-averaged vorticity ω_{ens} (sec^{-1}) for weak plunging breaking waves; from top to bottom at gauges G8, G10 (initial surf zone; left graphs), and gauges G21, G23 (inner surf zone; right graphs).
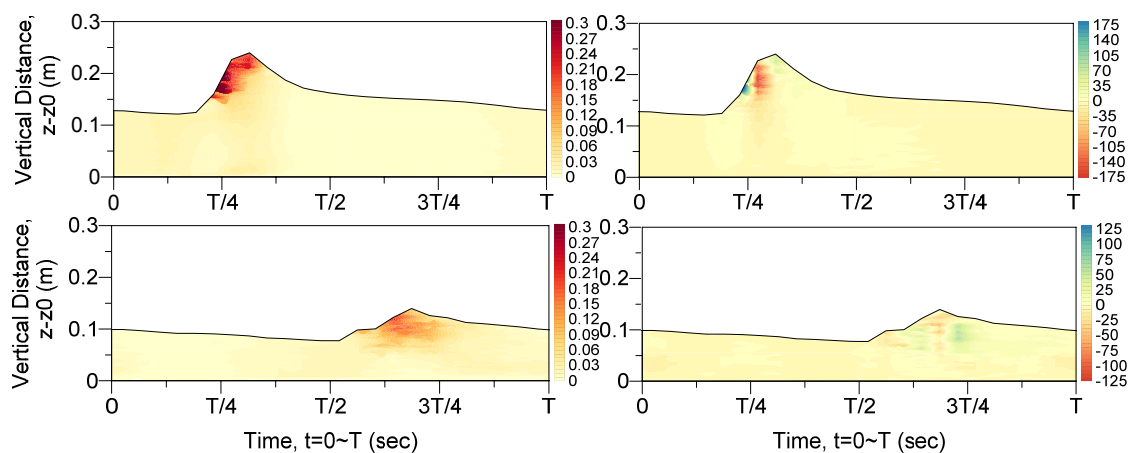

Figure 9. Simulated ensemble-averaged 2D TKE k_{ens} (m^2/sec^2) [left graphs] and shear stress $\tau_{ss,ens}$ (Pa) [right graphs] for weak plunging breaking waves at the incipient breaking region (G8; upper graphs) and inner surf zone (G21; lower graphs).

The shear stresses $\tau_{ss,ens}$, shown in Figure 9 (right graphs), revealed their extremes at the toe and the middle of the breaking wave front, with values ranging from -260 to 410 Pa. The maxima were obviously less than the normal stresses, shown with a similar way in Figure 10, as reported also in SF05. In the bore region, the respective values dropped to less than half of the initial ones, with magnitudes of about -170 to 185 Pa, but with small background magnitudes residing over the entire bore front, crest and back region. One could deduce that the Reynolds stresses distribution appeared to have a peak value in the lower part of the coherent structure, i.e. at the wave trough level, where large amounts of vorticity were

concentrated. This was consistent with the findings of Nadaoka et al. (1989), who described the mechanism of the instantaneous Reynolds stresses production, due to the downward motion of high velocity fluid during breaking near the wave trough. Contours of simulated ensemble-averaged horizontal and vertical normal stress $\tau_{nx,ens}$ and $\tau_{nz,ens}$ due to overall fluctuations in 2D are shown in Figure 10 (left and right graphs, respectively). The maxima of $\tau_{nx,ens}$=1100 Pa were traced at the breaking wave front (G8) and close to the crest everywhere else (450 Pa at G21). The contours of $\tau_{nx,ens}$ appeared to be very dense and have an almost elliptical shape in the incipient breaking region and then spread markedly as time progressed, while they appeared to be rather elongated under bores (G21). The same accounted for $\tau_{nz,ens}$ with contour patterns more elliptical in the initial surf zone and highly elongated for bores. However, the different spatial distribution near the crest, compared to $\tau_{nx,ens}$, indicated anisotropy of approximate turbulence, reported also in SF05.
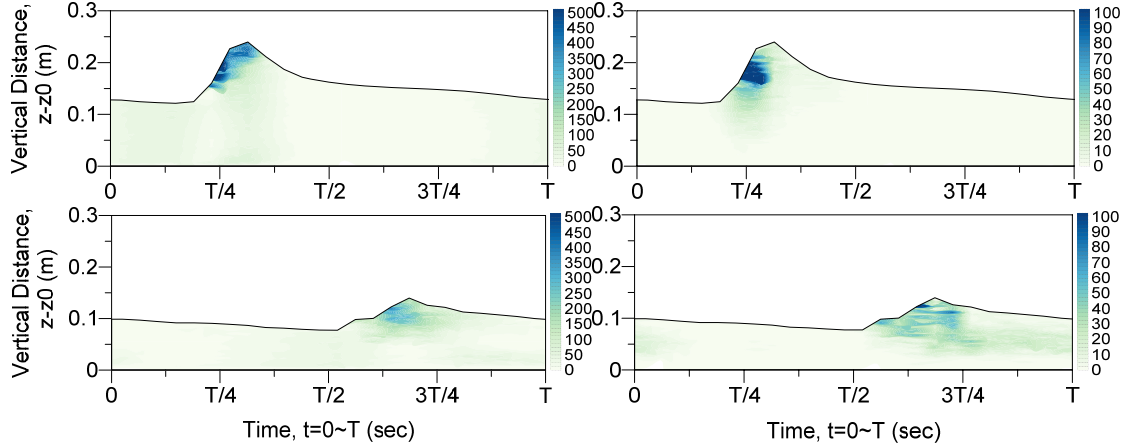

Figure 10. Simulated ensemble-averaged horizontal and vertical normal stress $\tau_{nx,ens}$ [left graphs] and $\tau_{nz,ens}$ [right graphs] (Pa) for weak plunging breaking waves at the incipient breaking region (G8; upper graphs) and inner surf zone (G21; lower graphs).
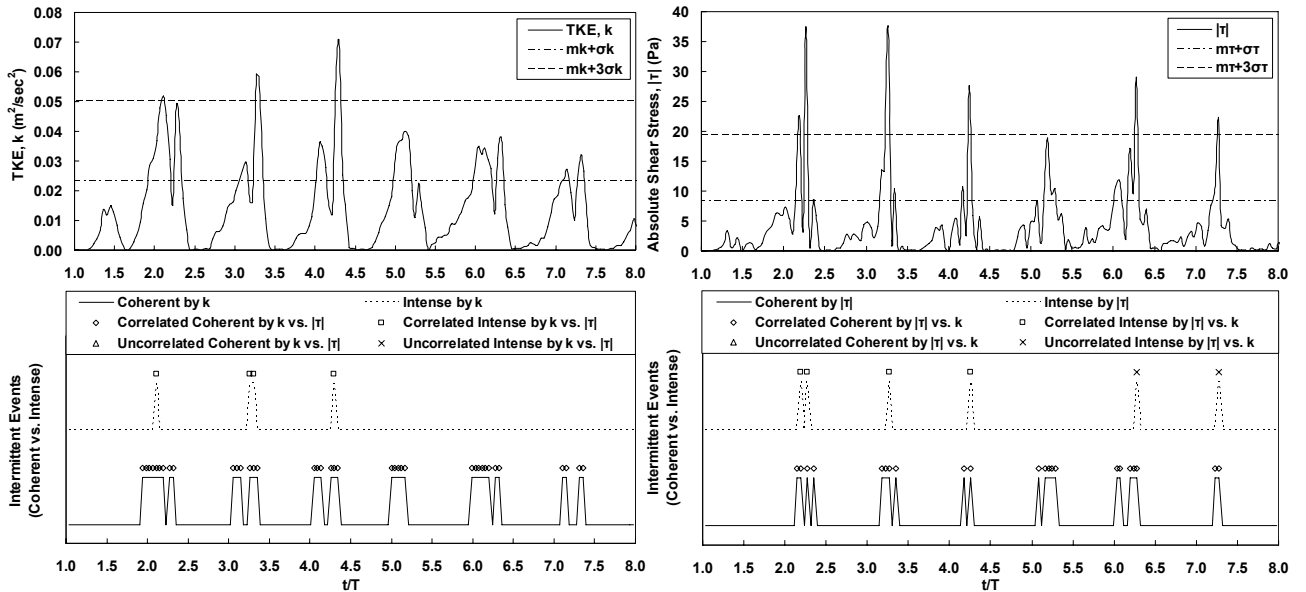
4.5 Intermittent events

Figure 11. Identification of intermittent events based on temporal variation of TKE k (left graph) and of absolute shear stress $|\tau_{ss}|$ (right graph), at mid-depth of the incipient breaking region (G8). Coherent and intense events thresholds are $m_k+\sigma_k$ and $m_k+3\sigma_k$ based on k; $m_\tau+\sigma_\tau$ and $m_\tau+3\sigma_\tau$ based on $|\tau_{ss}|$.

Identification of (coherent and intense) intermittent events for the fluctuating components of approximate turbulent features of the flow, was attempted according to Cox and Kobayashi (2000), by heuristically defining thresholds ($m+\sigma$ for coherent, $m+3\sigma$ for intense) based on the mean m and the standard deviation σ of the time-series of TKE k and absolute shear stresses $|\tau_{ss}|$ (Figure 11; upper graphs). Numerical measurements were taken at mid depth. The depth-averaged statistics of the coherent and intense events are presented in Table 2. It was found that intermittent coherent [or intense] events occur for a small portion N_{COH}<13% [or N_{INT}<3%] of the TKE time-series, but contribute significantly to its magnitude by containing a significant amount of all motions $(N \cdot m)_{COH}$>61% [or $(N \cdot m)_{INT}$>22%], in the entire surf zone. For the shear stresses intermittent coherent [or intense] events also occur infrequently N_{COH}<10.2% [or N_{INT}<3.2%] of the $|\tau_{ss}|$ time-series, yet define its magnitude by containing a significant amount of all motions $(N \cdot m)_{COH}$>63% [or $(N \cdot m)_{INT}$>24%]. In general, we can conclude that for TKE, 8~13 in 100 events are statistically coherent and correspond to 60~80% of the overall fluctuating motions. For the intense intermittent events of TKE, the analogies are even more pronounced. Namely, 1~3 intermittent in 100 events, account for almost 20~50% of the overall amount of fluctuating motions based on the TKE time-series. The shear stress time-series reveals analogous results. It is also observed that the proportion of intermittent

events is increased towards the inner surf zone compared to the incipient breaking region, while the corresponding amount of 2D turbulent motions decreases. Therefore, in the region of the propagating bore front, intermittent fluctuations, integrated throughout the water column, are comparable in size with the corresponding residual ones, which have remained from the passage of previous breakers.

The relationship of these intermittent coherent and intense signals was also examined with the use of conditional probabilities (Table 3), based on the lower graphs of Figure 11, which portray an graphical technique of identification and correlation of intermittent events of TKE against shear stresses and vice versa (Cox and Kobayashi, 2000). The correlation between τ_{ss} and k based coherent events decreases slightly as we go shoreward, while it increases for intense events. This indicates that the magnitude of the intense events increases landward in the surf zone, while the most frequent coherent events remain practically invariant. This is consistent with the breaking mechanisms and cross-shore sediment transport patterns of Cox & Kobayashi (2000).

Table 2. Depth-averaged percentages (%) of coherent N_{COH}/N and intense N_{INT}/N intermittent events and respective coherent $N_{COH} \cdot m_{COH}/N \cdot m$ and intense $N_{INT} \cdot m_{INT}/N \cdot m$ motions at specific gauges, based on k (upper part) and $|\tau_{ss}|$ (lower part).

Gauge	Coherent Events		Intense Events	
	N_{COH}/N (%)	$N_{COH} \cdot m_{k,COH}/N \cdot m_k$ (%)	N_{INT}/N (%)	$N_{INT} \cdot m_{k,INT}/N \cdot m_k$ (%)
G8	10.19	78.13	2.62	39.90
G10	8.54	74.38	1.65	47.69
G21	12.67	63.99	2.20	22.85
G23	9.50	61.09	1.79	26.72
Gauge	N_{COH}/N (%)	$N_{COH} \cdot m_{\tau,COH}/N \cdot m_\tau$ (%)	N_{INT}/N (%)	$N_{INT} \cdot m_{\tau,INT}/N \cdot m_\tau$ (%)
G8	7.02	73.19	2.07	41.67
G10	5.92	69.25	2.20	49.65
G21	10.19	63.07	1.93	24.61
G23	7.85	64.14	3.17	40.09

Table 3. Depth-averaged correlation percentages (%) of intermittent events at specific gauges, based on conditional correlation of k to $|\tau_{ss}|$ (upper part) and $|\tau_{ss}|$ to k (lower part).

Correlation of events relating	Gauges	Coherent Events		Intense Events	
		Correlated (%)	Uncorrelated (%)	Correlated (%)	Uncorrelated (%)
k to $|\tau_{ss}|$	G8	100.00	0.00	86.90	13.10
	G10	100.00	0.00	100.00	0.00
	G21	98.92	1.08	66.67	33.33
	G23	92.65	7.35	95.83	4.17
$|\tau_{ss}|$ to k	G8	98.55	1.45	88.89	11.11
	G10	98.67	1.33	83.33	16.67
	G21	98.41	1.59	94.44	5.56
	G23	96.03	3.97	60.71	39.29

5. CONCLUSIONS

A refined resolution SPH model was implemented, combined with a pseudo-LES approach of a Smagorinsky-type SPS technique for approximate (2D) turbulence closure, in order to simulate the period-averaged kinematics, ensemble-averaged, and instantaneous turbulence in the surf zone created by a weak plunger. Numerical results of classic wave features compared very well against the experimental data of Stansby and Feng (2005). A combination of heuristic methods was proposed for the transformation of the scattered Lagrangian SPH data to Eulerian values at fixed nodal points (gauge locations), and the discrimination of coherent structures and intermittent events from ordered wave motions. Thorough analysis of the flow length scales was presented, based on mixing lengths of the flow (Cox et al., 1994), which helped us define proper spatial discretization for a pseudo-LES approach in 2D SPH. Thus SPS-SPH model yielded far better results than the inviscid shallow-water equations model used by Stansby and Feng (2005), for all the flow properties examined. Moreover, the wave-induced mean flows were qualitatively well reproduced compared to experiments. Simulations clearly portrayed the undertow and onshore drift regions, as well as 'streaming' near the bottom. The calculated fluxes over a wave period plausibly confirmed a naught balance of the cross-shore currents. Fourier spectral analysis for several harmonics of the fluctuating velocities revealed their isotropic character up to rather high frequencies only in shear intensified regions such as the free surface at the incipient breaking point. Anisotropy of 2D turbulence was obvious everywhere else in the computational domain and this was corroborated by the temporal evolution of the Eulerian field for the Reynolds stresses, reported also by Stansby and Feng (2005).

The heuristic approach for ensemble-averaging, based on the work of Nadaoka et al. (1989), combined with the high cut-off frequency implemented proved to be able in reconstructing the large-scale coherent structures. The large-scale

repetitive patterns of vorticity, traced by the SPS-SPH model, were reproduced in a satisfactory way as compared to respective experimental studies. Spatial discretization, smaller than the integral turbulence length scale, seemed to suffice for SPH simulations of coherent structures. Considerable amount of vorticity was generated at the front face of the breaking waves and then it was entrained by large scale structures, into the underlying flow field, just as reported by Nadaoka et al. (1989). Vorticity appeared to be significant at the toe of the surface roller and gained magnitude at the steep front of the plunger as well as at the initial bore front, but reduced rapidly after, as shown in the experiments by Stansby and Feng (2005). Entrainment of concentrated vorticity by large-scale structures from the wavefront into the underlying field was observed (Nadaoka et al., 1989), inducing elongated vortical layers along the surface of the bore. Coherent structures of anti-clockwise vorticity were also observed near the bed, both below the bore and in front of the pre-breaking roller, resembling a mixing layer similarly to what was reported in relevant physical simulations. The bottom-originated vorticity was found to affect the vertical velocity profiles especially at the boundary layer, causing the inversion of the flow (streaming). The derived Reynolds stresses were apparently anisotropic despite the relatively high frequency of record sampling for a numerical approach. Analysis of intermittency for the fluctuating kinematic components in the surf zone revealed that coherent (and intense) events occur approximately for 10% (and 3%) of the record but account for 60% (and 20%) of the total amount of motions. Statistics clearly indicated that these motions are infrequent, yet of great significance in contributing to turbulence, shear stresses and sediment transport.

Future research on the matter should focus on the reproduction of fully 3D coherent structures, such as obliquely descending eddies and/or braid-type and horseshoe structures under weak plungers. Thus an effort to bend the extremely time-consuming computations, involving tens to hundred of million particles, with the use of new 'parallel' versions of the SPHysics code was set as a standard prospective goal.

REFERENCES

Christensen ED. and Deigaard R. (2001). Large eddy simulation of breaking waves. *Coast. Eng.*, 42, 53-86.

Christensen ED. (2006). Large eddy simulation of spilling and plunging breakers, *Coast. Eng.*, 53, 463-485.

Cox DT. and Kobayashi S. (2000). Identification of intense, intermittent coherent motions under shoaling and breaking waves. *J. of Geophys. Res.*, 105(C6), 14223-14236.

Cox DT., Kobayashi N. and Okayasu A. (1994). Vertical Variations of Fluid Velocities and Shear Stress in Surf Zones. *Proc. 24th Int. Conf. Coast. Eng.*, 98-112.

Dalrymple RA. and Rogers BD. (2006). Numerical Modeling of Water Waves with SPH Method. *Coast. Eng.* 53, 141-147.

Farahani RJ. and Dalrymple RA. (2014). Three-dimensional reversed horseshoe vortex structures under broken solitary waves. *Coast. Eng.*, 91, 261-279.

Farahani RJ., Dalrymple RA., Hérault A. and Bilotta G. (2012). SPH modeling of mean velocity circulation in a rip current system, *Proc. 33rd Int. Conf. on Coast. Eng.*

Gómez-Gesteira M., Rogers BD., Dalrymple RA., Crespo AJC. and Narayanaswamy M. (2010a). *User Guide for the SPHysics Code v2.0.*

Gómez-Gesteira M., Rogers BD., Dalrymple RA. and Crespo AJC. (2010b). State-of-the-art of Classical SPH for Free-Surface Flows. *J. of Hydr. Res.*, 48, Extra Issue, 6-27.

Longuet-Higgins MS. (1953). Mass transport in water waves. *Phil. Trans. Roy. Soc. London A*. 245, 535–581.

Makris CV., Memos CD. and Krestenitis YN. (2011). Modeling of Breaking Wave Dynamics, Surf Zone Turbulence and Wave-Induced Mean Flows with the SPH Numerical Method. *Proc. 5th Int. Short Conf. on Applied Coast. Res. (SCACR)*. Aachen.

Makris CV., Krestenitis YN. and Memos CD. (2012). SPH modeling of plunging wave breaking, surf zone turbulence and wave-induced currents. *Proc. of 22nd Int. Offshore (Ocean) and Polar Eng. Conf. (ISOPE)*, Rhodes-Greece, 1204-1212.

Makris CV., Memos CD. and Krestenitis YN. (2014). On SPH Modelling of Surf Zone Turbulence Under Weak Plungers, *Proc. of 3rd International Association of Hydraulic Research Europe Congress*, IAHR, Porto, Portugal.

Monaghan JJ. (2005). Smoothed Particle Hydrodynamics, *Rep. Prog. Phys.*, 68, 1703-1759.

Nadaoka K., Hino M. and Koyano Y. (1989). Structure of the Turbulent Flow Field Under Breaking Waves in the Surf Zone, *J. Fluid Mech.*, 204, 359-387.

Pope SB. (2000). *Turbulent Flows*. Cambridge University Press.

Shao S. and Ji C. (2006). SPH Computation of Plunging Waves Using a 2-D Sub-Particle Scale (SPS) Turbulence Model, *Int. J. Numer. Meth. Fluids*, 51, 913-936.

Stansby PK. and Feng T. (2005). Kinematics and Depth-Integrated Terms in Surf Zone Waves from Laboratory Measurement, *J. Fluid Mech.*, 529, 279-310.

Svendsen IA. (1987). Analysis of surf zone turbulence. *J. Geophys. Res.* 92(CS), 5115-5124.

Ting FC. and Kirby JT. (1995). Dynamics of surf-zone turbulence in a strong plunging breaker. *Coast. Eng.* 24, 177-204.

Violeau D. (2012). *Fluid Mechanics and the SPH Method - Theory and Applications*. Oxford University Press.

Zhao Q., Armfield S. and Tanimoto K. (2004). Numerical Simulation of Breaking Waves by a Multi-Scale Turbulence Model. *Coast. Eng.* 51, 53-80.